Received: 19 April 2022 | Revised: 27 October 2022 | Accepted: 29 October 2022

DOI: 10.1111/ijac.14307

International Journal of Applied Ceramic Technology

RESEARCH ARTICLE

Effect of coupon geometry and preload on flexural properties of oxide ceramic matrix composites

Tobias Lehnert[1] | **Yuan Shi**[1] | **Daniel Cepli**[1] | **Raouf Jemmali**[1] | **Thomas Wamser**[2] | **Andreas Lauer**[2] | **Jan Roßdeutscher**[3] | **Britta Panthen**[3]

[1]Institute, of Structures and Design, German Aerospace Center Stuttgart, Stuttgart, Germany

[2]Schunk Kohlenstofftechnik GmbH, Heuchelheim, Germany

[3]Institute of Material Research, German Aerospace Center, Cologne, Germany

Correspondence
Tobias Lehnert, Institute of Structures and Design, German Aerospace Center Stuttgart, Pfaffenwaldring 38-40, Stuttgart 70569, Germany.
Email: tobias.lehnert@dlr.de

Funding information
European Union's Horizon 2020, Grant/Award Number: 686707

Abstract

Oxide ceramic matrix composites (O-CMCs) have a high potential for usage in thermal protection systems or combustion chambers because of their low weight, temperature- and corrosion stability as well as non-brittle failure behavior. Mechanical property changes over their lifetime due to operational loads are not well understood. Moreover, mechanical properties from planar samples under laboratory conditions often differ substantially from upscaled components with complex geometries. In this work, the influences of curvature and preloading conditions were investigated experimentally using modeling to determine boundary conditions. Effects of curvature and trends among preload conditions were determined, with high-cycle-fatigue-preload (HCF) reducing strength and Young's Modulus by 15% compared to their original values where low-cycle-fatigue-preload (LCF) had smaller effect. The low impacts of high temperatures and small-to-medium loads on the properties of O-CMCs makes them an interesting choice for high-temperature combustive environments.

KEYWORDS
ceramic matrix composite, engine components, mechanical properties, oxide fiber, preload

1 | INTRODUCTION

Oxide fiber-reinforced ceramic matrix composites (O-CMC) have been considered a key material for lightweight applications in corrosive oxidizing atmospheres above 1000°C.[1–3] Especially for mixer or exhaust cones of modern gas turbines, O-CMC benefit from good thermomechanical characteristics.[4,5] Industrial applications can be found in metallurgy or chemical industry, where the heat-treatment of metal parts or powders is relevant. Excellent thermo-shock behavior and the low mass of such materials enable energy-efficient processing and high product qualities.[6,7]

Most manufacturing processes of O-CMC are based on particle-loaded slurries that are used to infiltrate the fiber rovings. After drying and sintering, a porous matrix surrounds the fiber filaments. This microstructure is the reason for the non-brittle material behavior[8,9] due to the fact that cracks are deflected along the fibers because of the porous weak matrix system.[4,10] For an efficient production of complex-shaped O-CMC components, storable prepregs are an interesting opportunity. In this case, fabrics are

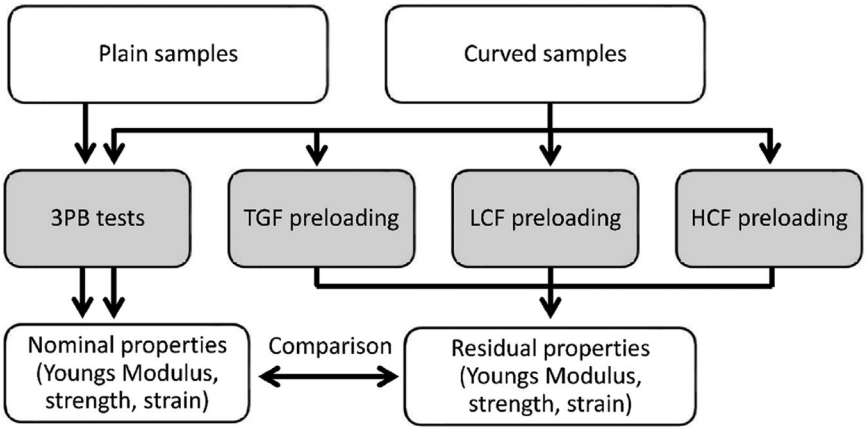

FIGURE 1 Overview of investigations in this paper

infiltrated with slurries. The layup of cut prepregs on molds with a subsequent consolidation in an autoclave leads to a green composite that is sintered next.[11,4]

The behavior of O-CMCs in a combustion environment was investigated by a handful of papers only. In Askarinejad et al.,[12] the influence of a combustive environment on the thermal fatigue of Nextel 720/alumina CMCs was investigated. Moreover, this study investigated the effects of defects inside the material. The defects were found to reduce fatigue life in a combustive environment by an order of magnitude. In Volkmann et al.,[13] a reduction of strength and stiffness of three O-CMCs based on Nextel 610 fibers was found for a sample exposure of 50 h under 1000 and 1200°C. For temperatures above 1100°C, Schmücker et al.[14] demonstrated a significant grain growth of the Nextel 610 fibers. Parthasarathy et al.[15] and Mattoni et al.[16] conducted studies on Nextel 720/A–based O-CMC heat shields that showed delaminations after exposure to more than 10 h with temperatures between 1200 and 1225°C. In Mattoni et al.,[16] samples cut from the heat shield after temperature exposure showed reduced tensile but increased shear strength. The study concluded that the increase in shear strength was the result of matrix sintering. Cantonwine et al.[17] showed that grain growth and filament-to-filament sintering reduce the tensile performance but increase creep resistance in O-CMCs.

As a relatively new material group, O-CMCs are often tested small scale under laboratory conditions using planar samples. However, by upscaling the samples to components that find real application, it becomes clear that certain reductions in material properties have to be made. This paper investigated the influence of curvature of the samples as well as the influence of different kinds of preloads on the mechanical properties of O-CMC. First, strength, Young's modulus, and the fracture strain of planar O-CMC samples under a three-point-bending load (3 PB) were examined and compared with the curved samples (nominal properties in Figure 1). Then, in order to imitate the typical thermomechanical loads in turbine engines, three different preloads were considered typical challenges for the application of O-CMC materials: low-cycle-fatigue-preload with several thousand cycles (LCF), high-cycle-fatigue-preload with over 10^6 cycles (HCF), and thermal-gradient-fatigue-preload (TGF). The effect of these three preloads on the residual properties of curved coupons was investigated afterward (residual properties in Figure 1). With this, the influence of each preload as well as the influence of sample geometry on the residual mechanical properties could be determined independently.

2 | MATERIALS AND METHODS

It should be noticed that all samples investigated in this work were tested as received condition without any further machining.

2.1 | Material

The investigated O-CMC material is a continuous Al_2O_3 fiber-reinforced composite with a porous matrix based on Al_2O_3 and ZrO_2. As reinforcement, 8-harness satin weave (8HS) satin fabrics with a weight of approx. 650 g/m^2 made of 3000 den Nextel610 rovings were used. For manufacturing of the composites, prepregs were prepared by dipping the fabrics in an aqueous slurry that contains organic processing aids and fine-grained oxide matrix particles with a bimodal particle size distribution. Powder composition with coarse Al_2O_3 and fine ZrO_2-particles enables sintering porous matrices at low temperatures with no shrinkage. This is necessary because alumina fibers withstand shrinkage and degrade if sintering temperatures are too high. Slurry-infiltrated fabrics were dried to reduce water content that results in a storable prepreg. The produced prepregs are suitable for an autoclave processing.

TABLE 1 Density, open porosity, fiber volume content (FVC), and number of samples of planar (P1–P4) and curved samples (C1–C3)

Batch	Thickness (mm)	Density (g/cm^3)	Open Porosity (%)	FVC (%)	Number of samples
P1	2.78	2.99	26.88	44.9	8
P2	2.68	3.06	24.89	46.5	8
P3	2.66	3.03	25.56	46.9	8
P4	2.88	2.97	27.32	43.3	6
C1	2.42	2.9	29.78	38.7	8
C2	2.54	2.83	31.07	36.8	6
C3	2.25	2.87	30.03	41.6	7

For the mechanical investigation, a given number of cut prepregs are stacked up in 0/90° orientation either on a flat or curved mold and pressed to size with autoclave. Dried green bodies can be demolded and put into the sintering furnace at about 1200°C to solidify the matrix.

In total, seven batches were investigated in this work, from which three batches were manufactured with curvature (Table 1, C1–C3 with 220 × 200 mm^2 and diameter = approx. 250 mm) and four batches were manufactured as planar samples (Table 1, P1–P4 with 350 × 500 mm^2). The density, open porosity, and fiber volume content (FVC) of each batch were determined, and the results are summarized in Table 1. The FVC of O-CMC was calculated by the measurement of the initial weight of the Al_2O_3 fibers and the total volume of the finished component. The density and porosity of the manufactured plate were measured using the Archimedes method,[18] which was carried out on the component before sample cutting. It can be noted that density deviated slightly throughout all batches even considering curved and planar samples with slightly higher values for planar samples (5%). Porosity was slightly higher in curved samples (13% increase compared to planar samples), and FVC and thickness were generally greater in the planar samples (16% FVC-increase of planar samples compared to curved samples).

2.2 | Mechanical tests

2.2.1 | Three-point-bending test (3 PB)

The mechanical properties of O-CMC material were determined and evaluated under 3 PB load with and without preload at room temperature in air under quasi-static loading.

The planar samples with the fiber orientation 0°/90°, which was investigated only without preload, were cut from flat plates using a diamond saw. After cutting, the samples were cleaned with water using an ultrasonic bath and then dried in a drying cabinet at 110°C. The dimensions were roughly 90 × 10 × 2.7 mm^3, and the thickness of each batch is shown in Table 1. The 3 PB-tests were carried out using a universal testing machine Zwick Roell UTS 10 with a 2.5 kN load cell from A.S.T. type KAF-TC. The displacement was measured with a Millitron 1310 system. Three inductive probes (at the center and additionally at −15 and +15 mm from the center) were used to determine only the displacement of the specimen without any displacement of the fixtures or the loading system. The test configuration can be seen in Figure 2A. The support span was 80 mm with a testing speed of 2 mm/min. In order to achieve the desired tensile or compression failure mode as described in[19] for the 0°/90° fiber orientation bending specimens with a span length to thickness ratio of $L/t \sim 26$ were used to avoid delamination (interlaminar shear failure). The bending strength is determined from the maximal stress reached during a single test.[19] Young's modulus was determined using a linear fit for a defined stress interval (20–30 MPa) in the linear elastic region of the stress–strain curves.

The samples with curvature were cut from curved plates with a fiber orientation of 0°/90° using a diamond saw and then investigated with and without preload. The radius of curvature was 120.5 mm, and the dimensions of the samples were 90 × 10 × 2.4 mm^3. Due to the limited plate size, the ratio of span length to thickness is 20. The test setup for the curved samples is shown in Figure 2B. The thickness of each batch is summarized in Table 1. The test was conducted up to a failure of each sample on a universal testing machine Zwick 1494, and the test setup is shown in Figure 2B. The stress values and strength of curved coupons can be calculated through the analytical method, and the detail is explained in Section 3.2. For the measurement of strain, the longitudinal strain gauge was glued on the tensile site of bending specimens. Young's modulus was evaluated using a linear fit of the initial linear region from 20 to 30 MPa.

As mentioned above, in order to investigate the effect of preload on the mechanical properties of O-CMC, three mechanical preloads (LCF, HCF, and TGF) were conducted at first. Then, the residual properties of curved coupons inclusive strength, Young's modulus, and fracture strain were determined subsequently through 3 PB-test. The different preloads are explained separately in this section.

2.2.2 | Thermal-gradient-fatigue preload (TGF)

During the TGF test, a thermal gradient was induced between the two opposing sides of the curved

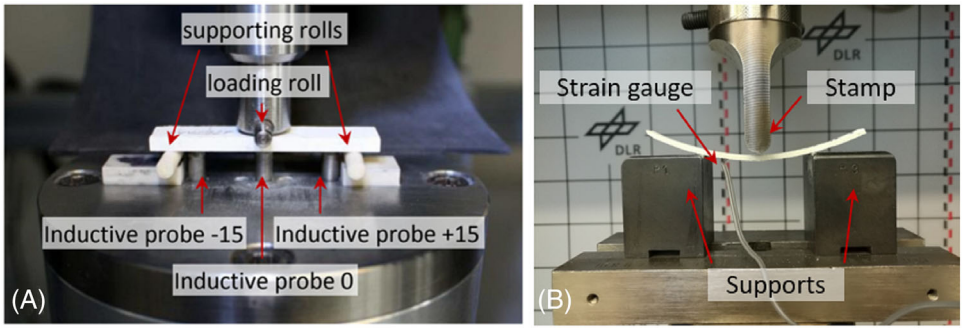

FIGURE 2 Test configuration for testing of (A) planar and (B) curved 3 PB specimens

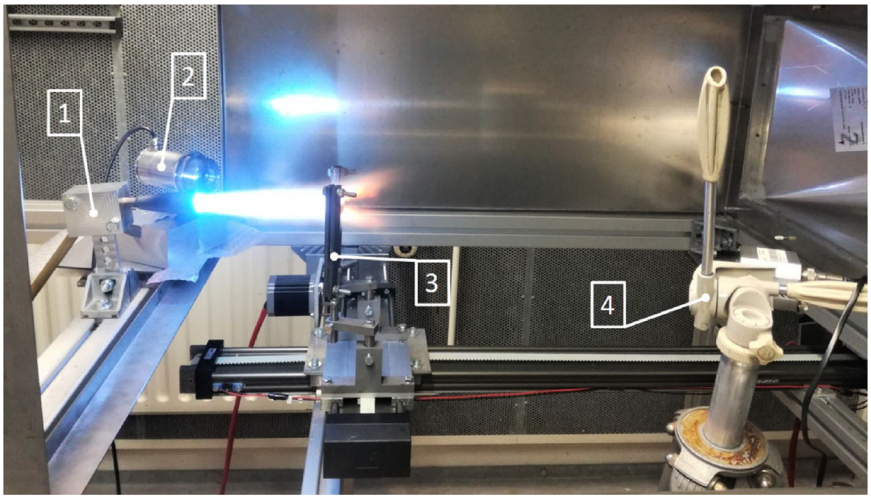

FIGURE 3 Acetylene-oxygen burner rig; (1): nozzle, (2): infrared thermometer (CTLaser MT), (3): mount with sample, (4): infrared camera Optris PI 450

sample, using an acetylene-oxygen burner rig, as shown in Figure 3. The temperatures during the tests were measured by optical measurement devices that were calibrated beforehand using thermocouples. The emissivity at different temperatures was determined for each device for a temperature range of 0–1000°C using curved samples.

Each sample was driven into and out of the flame five times. Between each cycle, the samples were cooled down to room temperature. In order to create a specific stress value in the sample, the resulting stresses corresponding to time in flame were calculated through simulation, as discussed in Section 3.1. As mentioned before, after the samples were subjected to five thermal gradient cycles, they were tested subsequently under 3 PB loading at room temperature in order to determine their residual mechanical properties.

2.2.3 | Low-cycle-fatigue preload (LCF)

The LCF preload was conducted using the same testing equipment as 3 PB for curved samples (Figure 2B). The LCF preload differed from the 3 PB-tests in applied force and cycle count. For each LCF sample, a stress level was calculated via curved beam theory as discussed in Section 3.2. The force necessary to obtain this stress level was calculated beforehand and set at the testing machine. The amount of loading cycles used in LCF tests was $n = 6000$ while using a feed speed of 30 mm/min. Similar to the TGF preload, the sample with LCF preload was tested for residual mechanical properties under 3 PB loading.

2.2.4 | High-cycle-fatigue preload (HCF)

The HCF-tests were carried out on a vibration test system TV 57315/LS-340 (TIRA Schwingtechnik Vibration Test Systems), hereinafter described as "shaker." The sample was positioned on a mount that used an adjusting screw and an adapter piece to hold it in place as shown in Figure 4. A laser system measured the amplitude of the free-swinging edges of the samples; acceleration was measured via an accelerometer. The amplitude of the edges was measured at a defined location that was marked on the sample before testing. Moreover, damping of one sample per batch was determined via the half-power-bandwidth

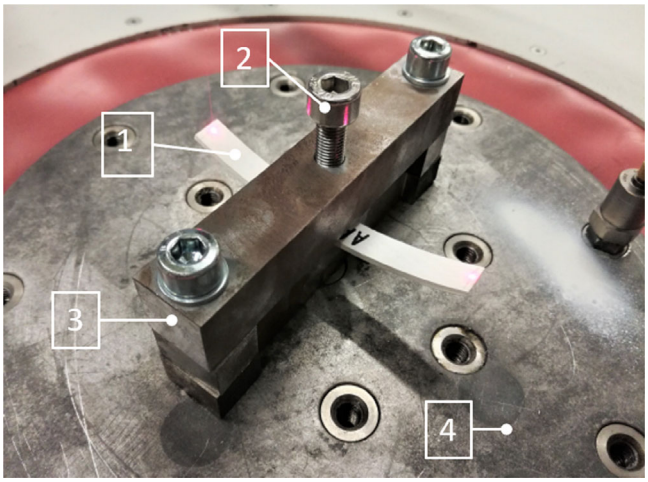

FIGURE 4 Oxide ceramic matrix composites (O-CMC) sample mounted on shaker for high-cycle-fatigue (HCF) preload, (1): curved sample, (2): mounting screw with adapter below, (3): mount, (4): shaker table

method. Modal and harmonic analyses were performed as discussed in Section 3.3.

At first, a frequency test run was done in order to search for natural frequencies of the sample. For this, frequencies between 0 and 3000 Hz were induced, and the amplitude response was recorded via laser. This yielded the first three natural frequencies of the sample, from which the second natural frequency was of interest because of the similar stress distribution compared to 3 PB-tests. Through simulation, the stresses in the sample could be determined as a function of amplitude of the sample edges. Thus, the practical tests were regulated via amplitude. The given amount of load cycles for each sample was $n = 10^6$.

3 | SIMULATIONS AND ANALYTICAL CALCULATIONS

The thermal and mechanical simulations were run using Ansys Workbench 17.2. All used material data were collected in mechanical tests from this work.

3.1 | Thermo-mechanical simulations of TGF

The thermomechanical tests were accompanied by transient thermomechanical simulations in order to calculate the necessary time in flame. Therefore, a virtual sample was subjected to a heat flux as shown in Figure 5, which resulted in a temperature distribution as shown in Figure 6. This heat flux was then tweaked until the simulated temperature distribution on the sample surfaces (convex and concave side) matched the temperature distribution of the practical test as shown in Figure 7. The sample was then held in place using fixed supports that simulated the real mount. The resulting stresses were then evaluated in the middle of the sample and plotted over time. An example for the stress distribution at a certain point in time is shown in Figure 8. This calibration procedure was then repeated once for each batch. Thus, the time in flame necessary to get a certain stress level could be calculated for the tests.

3.2 | Analytical calculation of 3 PB and LCF for curved samples

For the 3 PB- and LCF preload of curved samples, analytical calculations were used to gain the necessary stress levels. Therefore, beam theory for curved beams was used; here the stress distribution over the thickness is not linear. To account for this nonlinearity, the factors k_i and k_a were introduced in order to calculate the bending stresses at the sample surfaces.

The bending stresses were calculated as follows:

$$\sigma_i = k_i \cdot \frac{12M_b}{bh^3} \cdot c \tag{1}$$

$$\sigma_a = k_a \cdot \frac{12M_b}{bh^3} \cdot c \tag{2}$$

where M_b is the bending torque, c is the maximum distance of outer fiber to neutral fiber, and k_i and k_a are calculated as follows:[20]

$$k_i = \frac{c}{3 \cdot r}\left(\frac{c}{m \cdot r_i} - 1\right) \tag{3}$$

$$k_a = \frac{c}{3 \cdot r}\left(\frac{c}{m \cdot r_a} + 1\right) \tag{4}$$

The coefficients r_i and r_a are the inner and outer curvature radii of the sample. The coefficient m is calculated as follows:

$$m = -1 + \frac{r}{2c} \cdot \ln\left(\frac{r+c}{r-c}\right) \tag{5}$$

Because of the high curvature radius of the tested samples, the influence of k_i and k_a is very small (<2%). Nonetheless, these factors were taken into consideration when calculating the stress levels for all samples. To gain the real stress distribution, compression stresses were therefore multiplied by k_a factors between 1.0 and 1.02; tensile stresses were multiplied by k_i factors between .98 and 1.0 depending on the sample geometry.

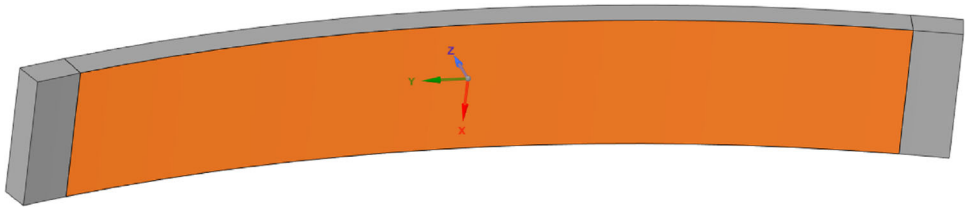

FIGURE 5 Boundary conditions of FEM simulation; the orange area was subjected to a heat flux that was then calibrated to match the observed temperatures. The gray areas on the sample edges were fixed to ensure comparable boundary conditions to the practical tests.

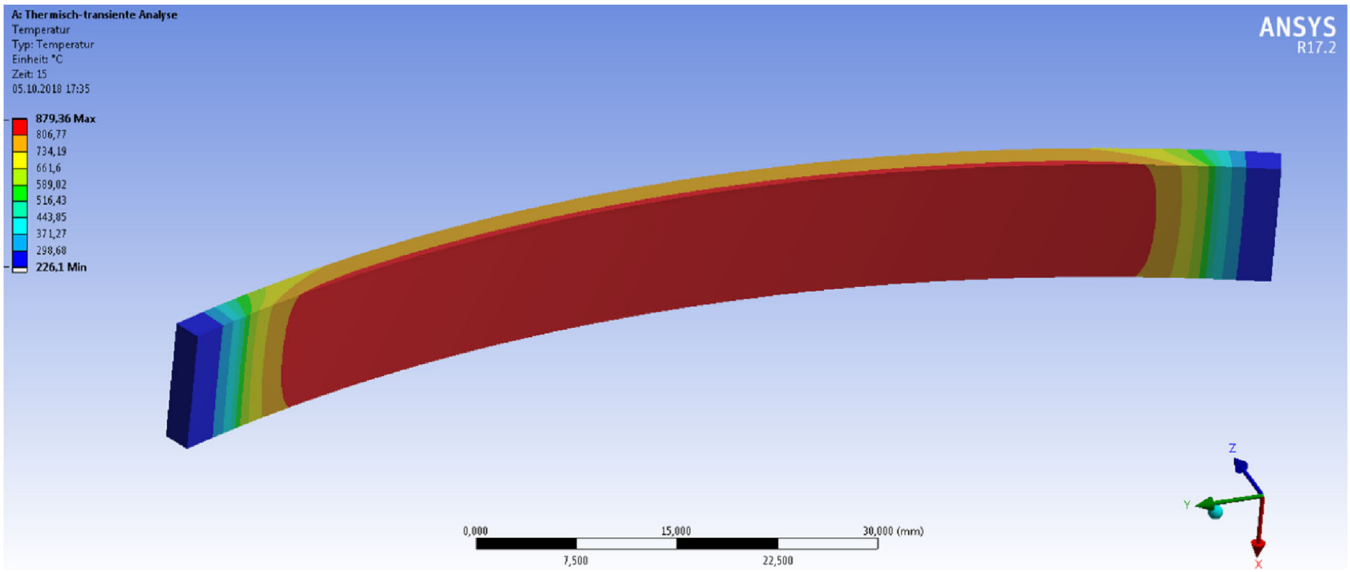

FIGURE 6 Resulting simulated temperature field. The heat flux was tweaked until the sample showed the same temperature distribution on both sides as observed with the infrared devices.

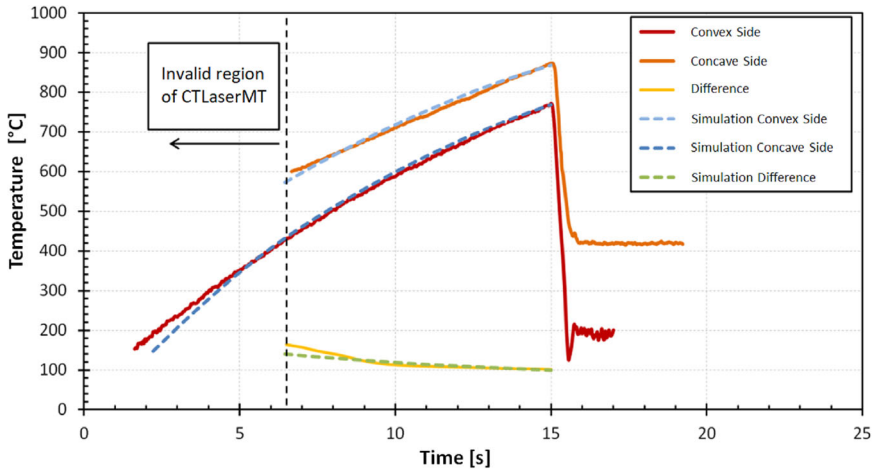

FIGURE 7 Simulated and real temperature distributions from both sides of the sample, flame was deactivated after 15 s; the valid temperature regime of the infrared thermometer CTLaserMT starts at 600°C, lower temperatures cannot be measured.

3.3 | Simulation of LCF and HCF preload

Modal and harmonic analyses were run in Ansys Workbench 17.2 in order to calculate the deformations, natural frequencies, and arising stresses in the samples. The natural frequencies were in good accordance with the practical tests and were used to determine the desired eigenmodes. The stresses in the sample could be calculated as a function of the amplitude of the sample edges. Therefore, damping had to be measured via the half-power

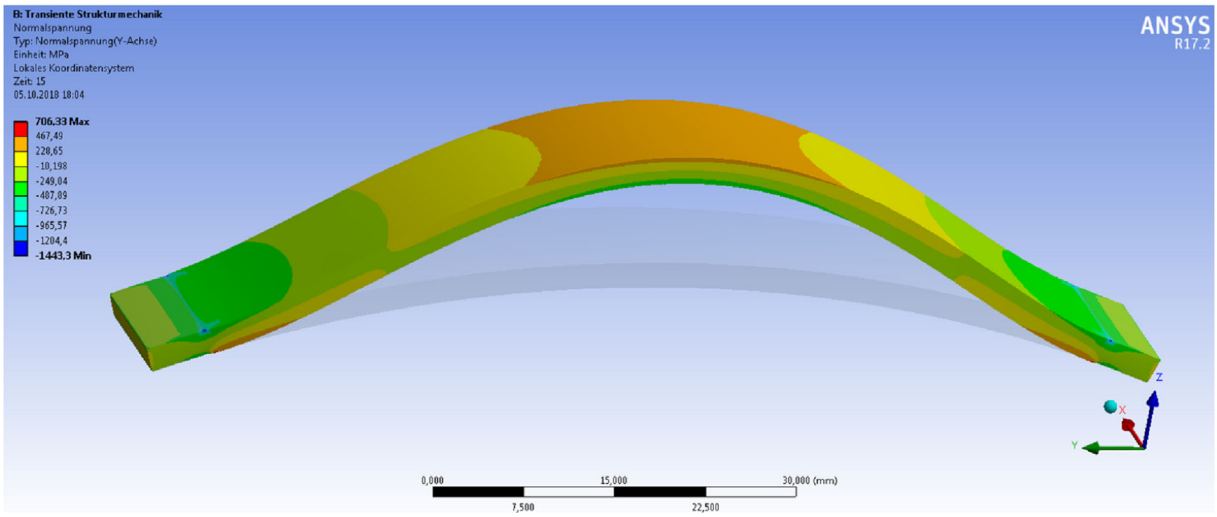

FIGURE 8 Calculated thermal stresses for the calibrated heat flux; shown deformations are exaggerated.

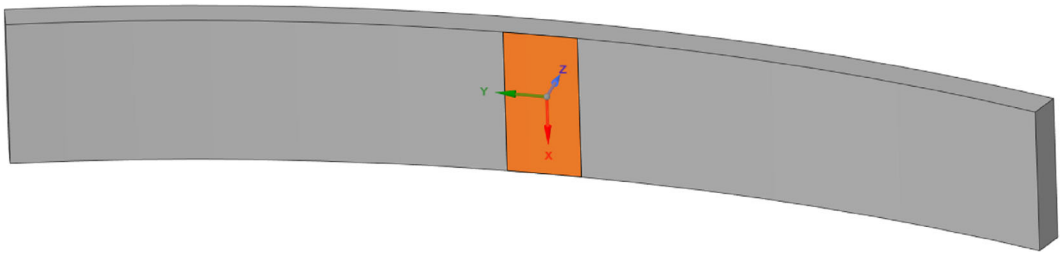

FIGURE 9 Boundary conditions of the high-cycle-fatigue (HCF)-test simulation; the orange area and its counterpart on the convex side of the sample were fixed in order to replicate the test setup conditions. The setup was then subjected to a modal analysis in order to calculate the natural frequencies as well as the resulting stresses for a given amplitude.

bandwidth method and was then considered in the simulation. Hence, the necessary amplitude in order to get a desired stress in the sample could be achieved by comparing simulated and measured amplitudes and then using the simulation to gain the stresses.

Figure 9 shows the area that was used to constrain the sample in the HCF simulations. Figure 10 shows the shape of the first five calculated eigenmodes of an HCF-sample. The second mode was set as a target mode due to its similarity in deformation compared to a 3 PB-test. After determining the damping coefficient through a practical shaker test, the stresses which occur during the second mode can be calculated for a given excitation acceleration. The resulting stress distribution for a given excitation acceleration as well as a damping coefficient is shown in Figure 11. Due to the fixed contact, a stress singularity forms at the edge of the contacting elements. Therefore, the stresses were evaluated 3 Elements away from the singularity.

4 | RESULTS AND DISCUSSION

4.1 | Effect of sample geometry: planar and curved samples

As mentioned before, due to the limited plate size, the span length to thickness ratio of curved coupons ($\frac{l}{d} = 20$) is slightly smaller than the planar samples ($\frac{l}{d} = 26$). However, it is reasonable to assume that the influence of this difference could be neglected, because the effect of interlaminar shear stress between the loading and supporting rollers should be negligible if the ratio is higher than 20.[19] Therefore, the discussion of effect of coupon geometry on the mechanical properties focuses on the production-related difference such as porosity or FVC of samples with and without curvature.

The results obtained from the 3 PB-tests of four different batches of planar samples (P1–P4) are summarized in

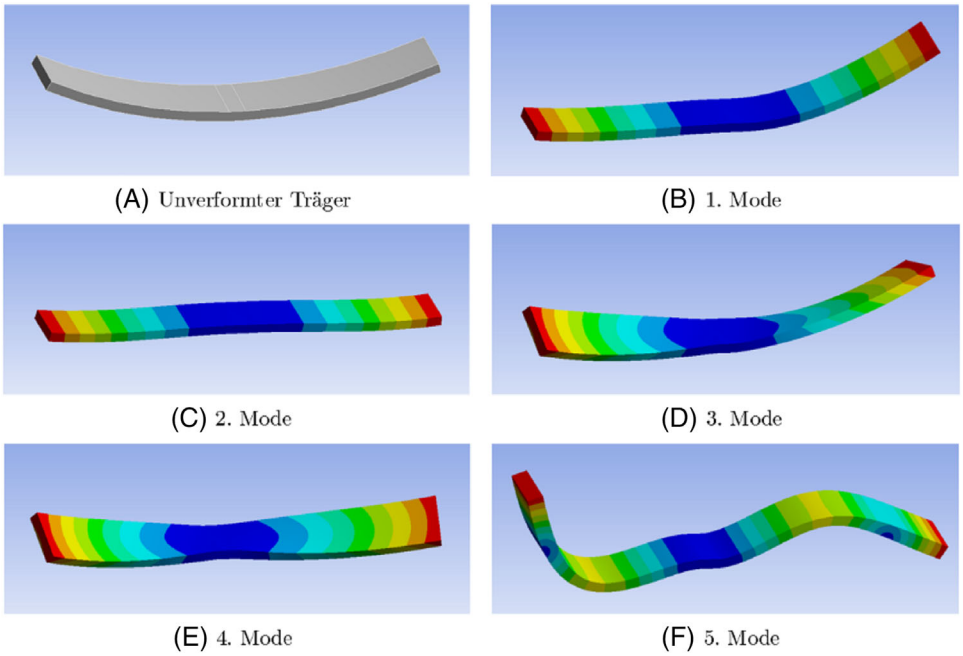

FIGURE 10 Eigenmodes of the sample during high-cycle-fatigue (HCF)-test (color scheme shows magnitude of deformation); the second mode was selected as target mode. (A) Undeformed sample, (B) First 1. Eigenmode, (C) 2. Eigenmode, (D) 3. Eigenmode, (E) 4. Eigenmode, (F) 5. Eigenmode

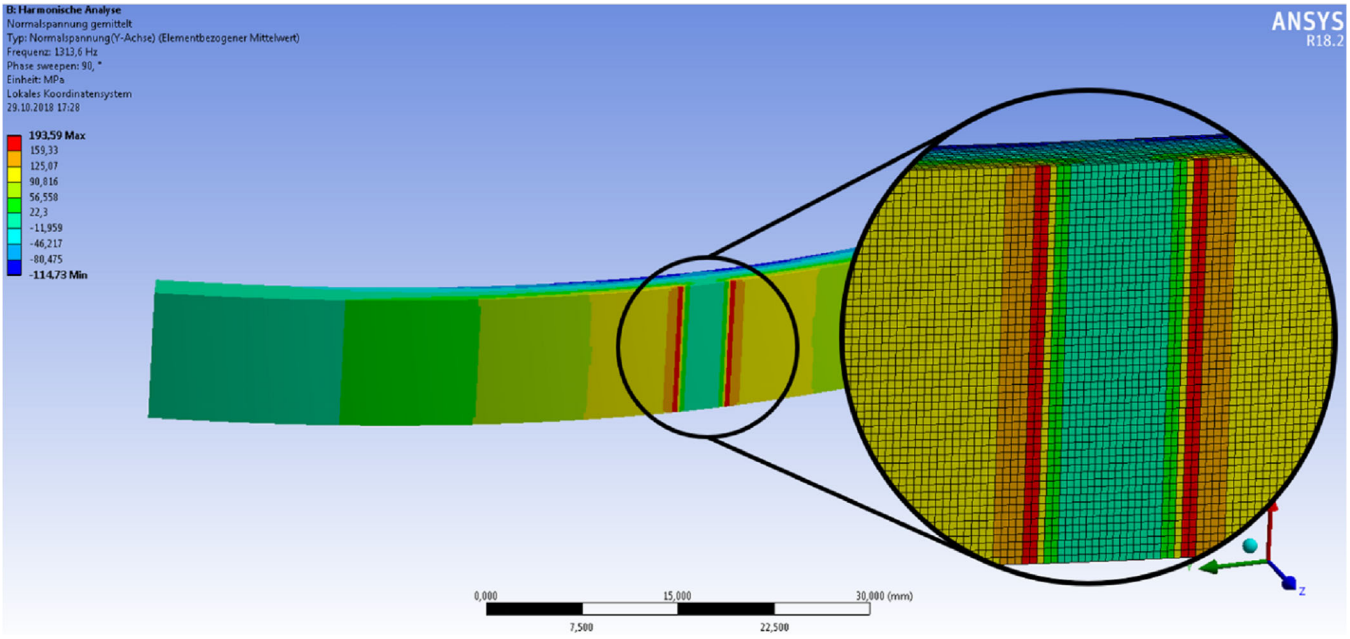

FIGURE 11 Stress distribution determined for a given damping coefficient and excitation acceleration

Table 2. Batch P4 shows slightly lowered strength values together with increased ultimate strain compared to the other batches. This was attributed to the slightly lower FVC in conjunction with a minor increase in porosity.

The greatest difference between planar and curved samples is the 3 PB-strength, where mean values for planar samples were about 25% higher, whereas the fracture strain of planar samples was about 39% higher as shown in Table 3. Young's moduli did not differ significantly. Young's moduli were determined using linear regression for stress–strain value pairs inside a defined stress interval (10–20 MPa for curved and 20–30 MPa for planar samples)

TABLE 2 Properties of planar samples determined in 3 PB-test

No. plate	σ_U (MPa)	ε_U (%)	E_{bend} (GPa)
P1	388 ± 18 (8)	.463 ± .032 (8)	110 ± 5 (8)
P2	372 ± 15 (8)	.455 ± .040 (8)	105 ± 6 (8)
P3	355 ± 22 (8)	.434 ± .052 (8)	107 ± 5 (8)
P4	367 ± 14 (6)	.499 ± .015 (6)	95 ± 11 (6)

in the linear elastic region of the stress–strain curves. The differences in the evaluation regimes are due to a preload that was used in the testing of the planar specimens. The preload of 8 N corresponds to a stress of 12–16 MPa, depending on the specimen cross section. For this reason, the stress interval of 20–30 MPa was chosen for the evaluation of Young's modulus.

The difference in strength between planar and curved samples can probably be explained by the overall higher FVC of planar samples and therefore greater number of fibers in tensile direction (average FVG in planar samples is 6% higher). Moreover, the manufacturing process of the curved geometry is more sensitive to flaws like wrinkling defects. Furthermore, the lower porosity and density of the planar samples benefit higher strength values (average porosity in curved samples is 4% higher; average density in planar samples is 5% higher). It can be observed that the fracture strain in planar samples is higher, which can be explained by slightly lower Young's modulus and production influences.

4.2 | Effect of preloads: LCF, HCF, and TGF

All in all, 54 curved samples from 3 different batches were subjected to preloads before testing. Planar samples were not subjected to preloading. The effects of preloads were determined through a subsequent 3 PB-test, as described earlier. It can be concluded that the observed effects of preloading on residual strength and stiffness were relatively small, ranging between 0% and −15.5%, if the preloading did not lead to failure during the preloading process. Regarding the scatter of strength, Young's modulus, and fracture strain for the samples without preloading that lies between 6% and 12%, the impact of preloading has to be considered minor.

In some cases, the samples experienced fracture during the preloading process; thus, there was no possibility for a subsequent 3 PB-test. This concerned 5 of the 11 LCF-preloading tests when a stress level of $\sigma = 200$ MPa was applied. The samples were taken from three different batches as shown in Table 4. In all other cases, there was no fracture during preloading. The residual strength

TABLE 3 Influence of curvature—comparison of curved and planar samples without preloading. The mechanical properties were determined through 3 PB-tests

	Mechanical Properties	
	Planar samples	Curved samples
3 PB-strength (MPa)	370 ± 17	291 ± 21
Young's modulus (GPa)	107 ± 5	110 ± 7
Fracture strain (%)	.46 ± .04	.33 ± .04
Material Properties		
FVC (%)	45.4	39.6
Porosity (%)	26.2	30.3
Density (g/cm^3)	3.0	2.9
Thickness (mm)	2.8	2.4

Abbreviations: FVC, fiber volume content.

TABLE 4 Tested samples versus failed samples during preloading for low-cycle-fatigue (LCF) tests with a stress level of $\sigma = 200$ (MPa) for all batches

Batch	Subjected to LCF preloading with $\sigma = 200$ (MPa)	Failed during LCF preloading with $\sigma = 200$ (MPa)
C1	4	1
C2	3	2
C3	4	2
All	11	5

of samples that survived the preloading with a stress level of $\sigma = 200$ MPa did not show a significant difference compared to the strength of the samples without preloading. The residual stiffness, on the other hand, showed a reduction of 12% compared to the samples without preloading. Figure 12 gives additional information about the loading cycle at which the samples failed during LCF tests corresponding to the stress-level to which they were subjected. Figures 13 and 14 give examples of typical stress–strain diagrams for run-out samples and samples which failed during preloading. In Figure 13, the sample showed basically no signs of stiffness reduction due to accumulated damage over 6000 loading cycles of $\sigma = 200$ MPa, which also held true for the residual properties gained from the eventual 3 PB-test. On the other hand, the sample shown in Figure 14 shows a significant reduction in stiffness as well as permanent strain already during LCF-preloading and eventually failed after 1400 loading cycles before reaching the end of the LCF test.

Residual strength, stiffness, and fracture strain were measured and compared against the properties of the 3 PB group without preloading. The results are shown in Figures 15 and 16. The numbers on the bars indicate the number of samples evaluated in each group;

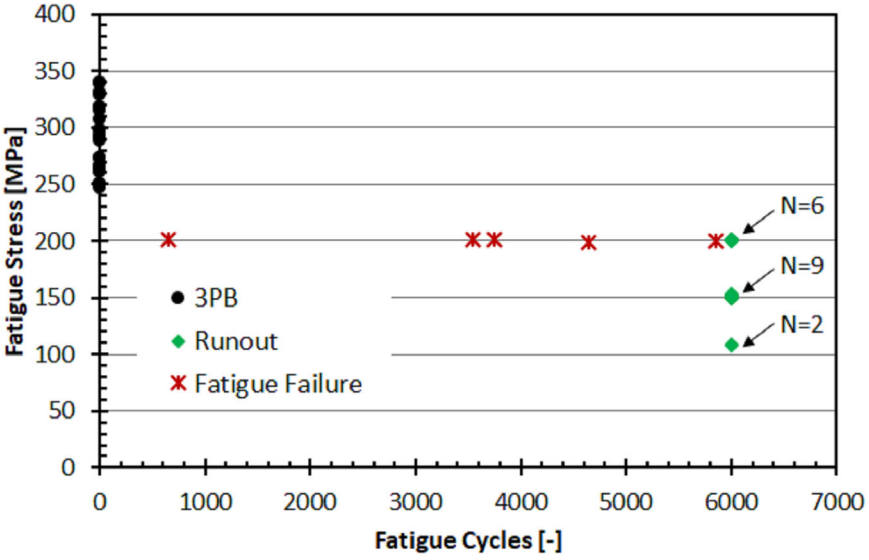

FIGURE 12 Low-cycle-fatigue (LCF) test results: stress level over loading cycle; a total of 5 out of the 11 tested LCF sample with a stress level of 200 MPa failed before reaching runout (6000 load cycles).

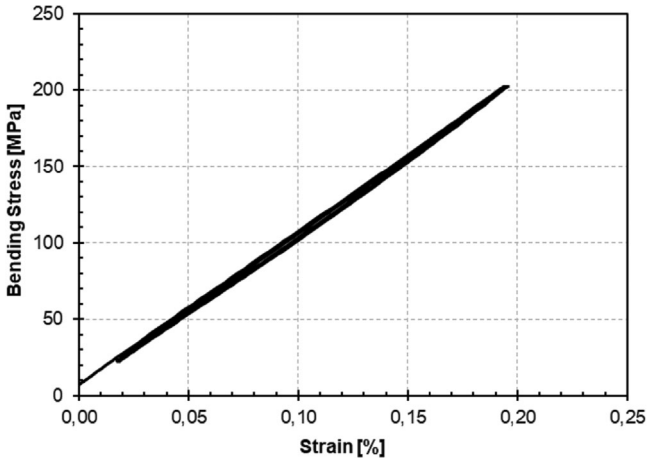

FIGURE 13 Example of a typical stress–strain curve from a sample that did not experience failure during preloading

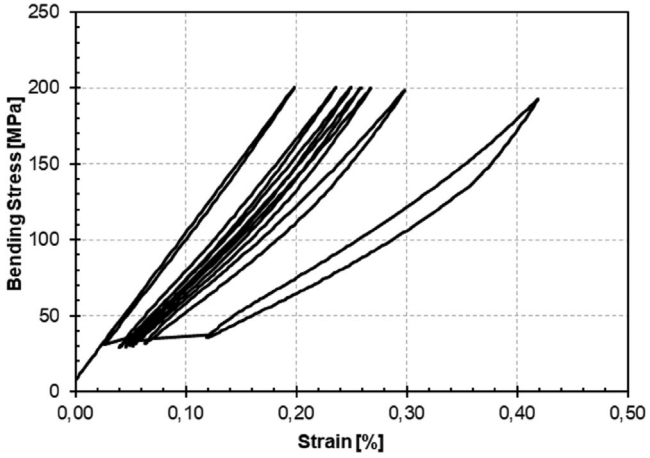

FIGURE 14 Example of a typical stress–strain curve that shows sample-failure during preloading (every 200th cycle is shown); a gradual loss of stiffness is noticeable until failure occurs after 1400 loading cycles.

numbers in brackets indicate the total numbers tested. The two numbers can differ due to various reasons. For the LCF tests, the difference is caused by samples that failed during preloading and, hence, could not be validated in a subsequent 3 PB-test. For 3 PB-tests, some samples had to be excluded from evaluation because they were located too close to the shell edges from which they were cut and, hence, showed strongly deviating mechanical properties. This is due to a decreased FVC in the edge regions, an effect that is caused by the manufacturing process.

The impact on Young's modulus is comparable throughout all preloading situations and amounts to reduced values of about 10%. The effect on strength is different for all groups of preloading.

It is noticeable that there was no measured loss in residual strength for samples, which survived the LCF test with a stress level of $\sigma = 200$ MPa, although only 6 out of 11 samples survived the process in the first place. Furthermore, LCF preloading with stress levels of $\sigma = 150$ and 110 MPa had only small impact on strength (4%–8%). This result is in accordance with the findings described in Refs. 21, 22 In Ref., 22 C/C–SiC samples were tested under LCF cycling up to 10^6 cycles, which even resulted in a small increase of tensile strength. This was explained partly due to an increased matrix crack density, which was not observed in this work, as explained later in Figure 17.

An HCF preloading had the biggest impact on sample strength; here the residual strength was reduced by 15.5% compared to samples without preloading. Although the applied stress level of 130 MPa was comparably low, the high number of 10^6 load cycles appeared to have a more significant influence on the properties. A microstructural investigation showed that the fracture surfaces of HCF and 3 PB samples displayed different failure

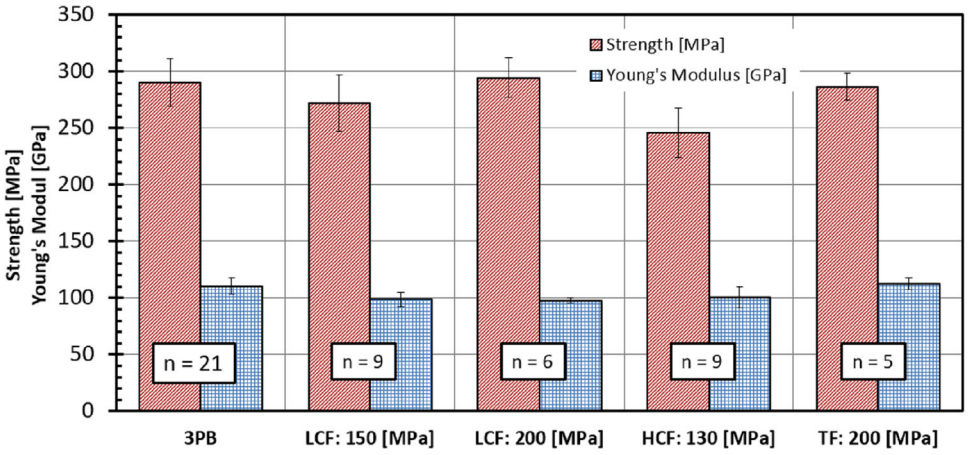

FIGURE 15 Comparison of residual strength and stiffness of samples with different preloads; numbers on bars indicate samples tested.

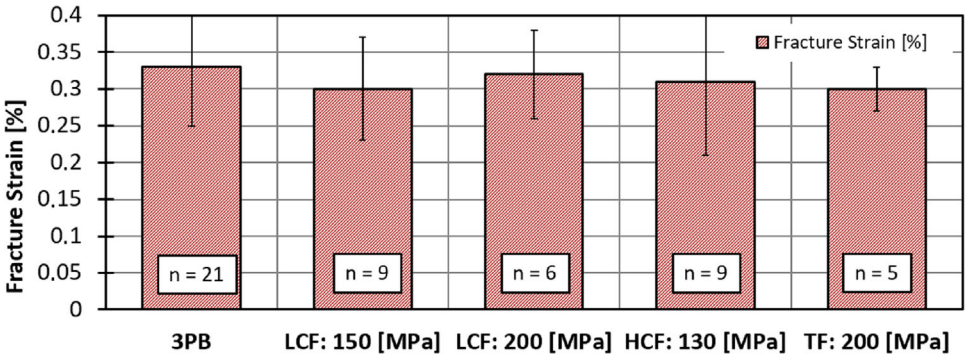

FIGURE 16 Comparison of fracture strain of samples with different preloads; numbers on bars indicate samples tested.

mechanisms as depicted in Figure 17. In samples that experienced HCF-preloading, fiber-bundle pullout was predominant in contrast to fiber-filament pullout, which is observed for the 3 PB and LCF samples. The decrease in fiber-filament pullout for high amounts of loading cycles is also observed in Refs. 23, 24 In Ref, 24 it is suggested that hindered interface sliding in the core of the specimen enables matrix cracks to propagate into the fibers causing brittle fracture. Moreover, the high porosity of the samples poses stress concentration spots that act as starting points for cracks under cyclic loading. The presence of cavities between fibers and matrix can also lead to fiber buckling during the unloading process,[25] which poses a possible explanation for the lowered strength.

TG-preloading did have almost no negative effect on residual strength. This is probably caused by the low number of loading cycles for the thermal tests ($n = 5$) compared to the other preloads. This theory is backed up by the fact that the same stress level of 200 MPa did also not lead to significant changes of mechanical properties in the first couple of load cycles in the LCF tests. Here damage accumulation resulted in a stiffness reduction after 1400–6000 load cycles for roughly half of the tested samples. Comparable thermal tests in literature describe similar results, like Dassios et al.[26] where preloading oxide CMC samples with a flame was found to even increase residual tensile strength by 20%. Mattoni et al.[16] described a small decrease of residual tensile strength of 10%–20% of samples cut from two N720/A heat shields that were subjected to 86 h of 1200–1225°C combustion environment. Here the higher temperatures as well as much longer exposure time can be expected to be the reason for the reduction in tensile strength. It should be noted that at the same time Mattoni et al.[16] reported an increase in the shear strength of comparable amount that was attributed to matrix sintering. In Askarinejad et al.,[12] a decrease of sample strength of around 10% was observed for samples subjected to cyclic tensile load while simultaneously heating with a combustion burner rig similar to the one used in this work. The reason for the more harmful impact on sample strength is probably due to the higher combustion temperatures of 1250°C as well as the combined thermomechanical load and the much higher amount of loading cycles ($n = 90000$).

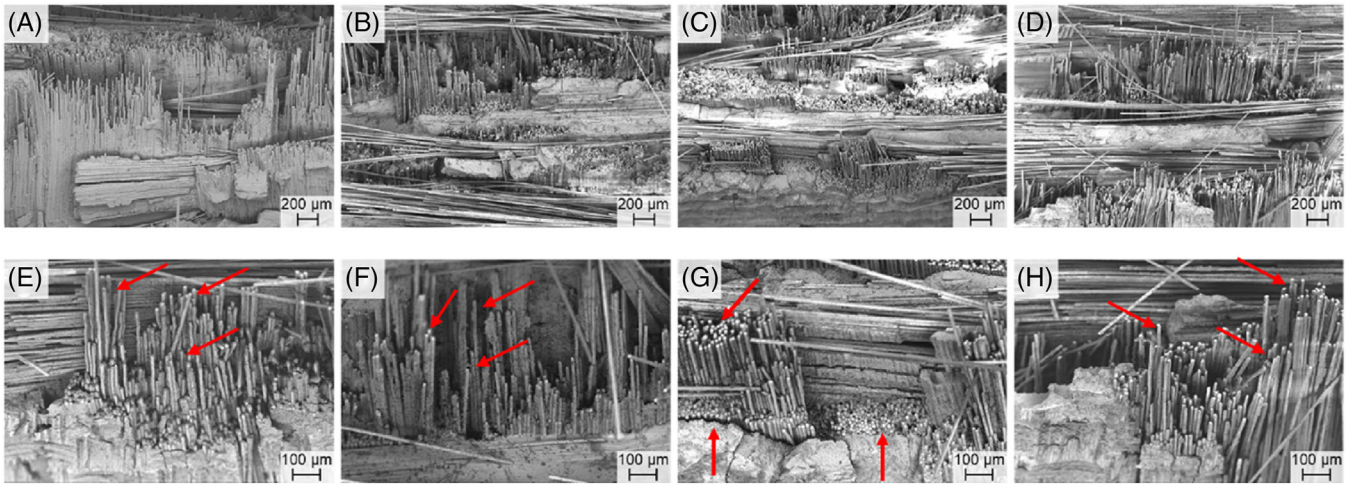

FIGURE 17 Scanning electron microscopy (SEM) images of the fracture surfaces of the curved samples after 3 PB-test. The letters define images of samples: (A and E) without preload, (B and F) with low-cycle-fatigue (LCF) preload, (C and G) with high-cycle-fatigue (HCF) preload, and (D and H) with thermal-gradient-fatigue (TGF) preload.

In Bansal and Lemon,[27] matrix densification and subsequent loss of porosity were named key drivers for lowered mechanical properties after long-term exposure to high temperatures. These mechanisms were not observed in this work probably due to the short exposure times.

In order to explain the effects of preload on flexural properties of O-CMC, the fracture surface of the failed samples was analyzed by means of scanning electron microscopy (SEM, Gemini Ultra Plus from Zeiss Group). The SEM images are summarized in Figure 17. At first sight, no considerable difference can be observed in the fracture surfaces of samples tested with and without preload (Figure 17A–D), as the four images show significant pullout effect. However, an enlargement of the position of sample with an HCF preload in Figure 17G indicates fiber bundle pullout (red arrows). On the contrary, fiber filament pullout effect is dominant in the case of sample without preload (Figure 17E) and with LCF and TF preloads (Figure 17F,H). These different fracture mechanisms can be considered the reason for the reduction of residual strength of HCF-preloaded samples. Given the high porosity stress peaks can form at the matrix pores, whereas the cyclic loading facilitates crack propagation. Because of the embrittlement, the composite loses the ability for stress redistribution,[28] and the matrix cracks can propagate into the fibers, which is more likely to happen for higher amounts of load cycles. Furthermore, the aforementioned fiber buckling effect gets worse for a higher amount of cycles. Samples with LCF and TGF preloadings show no significant differences in microstructure that is in good accordance with the very similar mechanical properties.

5 | CONCLUSIONS

In this paper, the mechanical properties of curved and planar oxide fiber-reinforced ceramic matrix composite (O-CMC) samples were examined during 3 PB-tests and compared against each other. Furthermore, the impact of LCF, HCF, and TGF preloadings on residual mechanical properties was investigated for the curved samples. The residual properties were determined by a subsequent 3 PB-test that followed all preloading-scenarios. The mechanical tests were accompanied by FEM simulations in order to determine the necessary loads to achieve predefined stress levels. In the case of the TGF-tests, the simulation was calibrated with the temperature fields observed by the infrared cameras. For LCF tests, a 3 PB setup functioned as a basis for the simulations. The HCF-tests required the determination of damping coefficients; here the simulations were calibrated by comparing and adjusting the measured natural frequencies and deformations while in resonance. To investigate the reason for the different impacts of preloading, microstructural SEM images were taken and evaluated.

Generally, it can be said that planar samples showed better mechanical properties compared to curved samples in all aspects but Young's modulus, where the values of planar and curved samples were comparable. This was mainly attributed to the higher FVC and lower porosity of the planar samples.

The influence of curvature and the corresponding deviating properties was also more significant than the influence of all tested preloads. Additionally, the scatter of Young's modulus (6%), strength (7%), and fracture strain (12%) of the curved samples was almost in the same range

as the influence of preloading, which ranged between 0% and 16%.

In the case of LCF preload with low stress levels up to 150 MPa, strength and Young's modulus reduced by only a small amount of less than 8% over 6000 cycles. For high stress levels of 200 MPa, roughly half of the samples failed during preloading, and the other half showed no signs of reduced mechanical properties. The low negative influence of cyclic preloading on the mechanical properties such as strength makes O-CMC interesting for thermal applications with low-to-medium mechanical loads. Thermal loading also showed barely any impact on residual mechanical properties. In this case, the low amount of load cycles is probably the cause as other literature reports a reduction in sample strength of about 10%–20% after subjection to higher loads or amounts of loading cycles.[12,16] This hypothesis is supported by the observation that the same stress level of 200 MPa caused a considerable amount of LCF samples to fail when several thousand load cycles were applied. The determination of residual properties of O-CMC samples in thermal combustive environments over a higher amount of load cycles poses an interesting topic for subsequent investigations.

Out of the applied preloading situations, HCF-tests seemed to have the largest negative impact on residual properties. Here an internal embrittlement was observed, which lead to fiber-bundle dominant failure instead of fiber-filament dominant failure that was observed in 3 PB and LCF samples. The embrittlement is probably caused by hindered interface sliding that enables matrix cracks to propagate into the fibers. Because of the high porosity of O-CMCs, cavities between fibers and matrix exist, which can cause fiber buckling during cyclic loading and act as starting points for matrix cracks.

A higher FVC as well as a higher density and lower porosity all seem to benefit mechanical properties.

Because of the complex nature of most manufacturing parts, deductions in mechanical values compared to laboratory conditions of planar samples have to be considered during the design process. Further investigation could uncover in greater detail why these deductions exist and how to minimize them. All in all, the high-temperature resistance as well as the high resistance to oxidation and low-cycle-fatigue loading makes O-CMCs an interesting candidate for applications in exhaust environments.

ACKNOWLEDGMENTS

The authors like to thank Marco Alexander Smolej, Felix Vogel, and Matthias Scheiffele at the DLR-Institute of Structures and Design for the collaboration and support for this work and Ferdinand Flucht at the DLR-Institute of Material Research for conduction of the 3 PB-tests of planar samples. We also thank Schunk Kohlenstofftechnik GmbH for the provision of the examined materials and MTU Aero Engines AG for the support of the above-mentioned project. This project has received funding from the Clean Sky 2 Joint Undertaking under the European Union's Horizon 2020 research and innovation program and under grant agreement No. 686707.

Open access funding enabled and organized by Projekt DEAL.

ORCID

Tobias Lehnert https://orcid.org/0000-0003-3319-8976
Yuan Shi https://orcid.org/0000-0002-4210-9069

REFERENCES

1. Bansal NP, editor. Ceramic matrix composites. Hoboken, NJ: John Wiley & Sons, Inc.; 2015.
2. Lewis D. Future opportunities and critical needs for advanced ceramics and ceramic matrix composites in aerospace applications. In: Jessen T, Ustundag E, editors. 24th annual conference on composites, advanced ceramics, materials, and structures: a ceramic engineering and science proceedings, Vol. 21(3). Hoboken, NJ, USA; 2000. p. 2–14.
3. Zawada LP, Hay RS, Lee SS, Staehler J. Characterization and high-temperature mechanical behavior of an oxide/oxide composite. J Am Ceram Soc. 2003;86:981–90. https://doi.org/10.1111/j.1151-2916.2003.tb03406.x
4. Shi Y, Hönig S, Frieß M, Rüdinger A, Pritzkow W, Koch D. Manufacture and characterization of oxide ceramic matrix composites out of commercial pre-impregnated fabrics. Ceram Int. 2018;44:2320–7. https://doi.org/10.1016/j.ceramint.2017.10.198
5. Volkmann E. Effects of high-temperature exposure on the mechanical performance of polymer-derived oxide-based ceramic matrix composites. Berlin: Elsevier; 2015.
6. Bansal NP, editor. Handbook of ceramic composites. Boston: Kluwer Academic Publishers; 2005.
7. Spriet P. CMC applications to gas turbines. In: Bansal NP, Lamon J, editors. Ceramic matrix composites. Hoboken, NJ, USA; 2014. p. 591–608.
8. Shi Y, Hofmann S. Determination of elastic properties for a wound oxide ceramic composite. J Ceram Sci Technol. 2014;5(1):31–8.
9. Zok FW. Developments in oxide fiber composites. J Am Ceram Soc. 2006;89:3309–24. https://doi.org/10.1111/j.1551-2916.2006.01342.x
10. Shi Y, Jain N, Koch D. Investigation and modeling of tensile failure properties of wound ceramic matrix composites. Composites, A Appl Sci Manuf. 2018;114:316–26. https://doi.org/10.1016/j.compositesa.2018.08.029
11. Gerendás M, Cadoret Y, Wilhelmi C, Machry T, Knoche R, Behrendt T, et al. Improvement of oxide/oxide CMC and development of combustor and turbine components in the HiPOC program. In: Aircraft engine; ceramics; coal, biomass and alternative fuels; wind turbine technology, Vol. 1, ASME and Rolls-Roys Deutschland Ltd & Co KG; 2011. p. 477–90.

12. Askarinejad S, Rahbar N, Sabelkin V, Mall S. Mechanical behavior of a notched oxide/oxide ceramic matrix composite in combustion environment: experiments and simulations. Compos Struct. 2015;127:77–86. https://doi.org/10.1016/j.compstruct.2015.02.040
13. Volkmann E, Tushtev K, Koch D, Wilhelmi C, Göring J, Rezwan K. Assessment of three oxide/oxide ceramic matrix composites: mechanical performance and effects of heat treatments. Composites, A Appl Sci Manuf. 2015;68:19–28. https://doi.org/10.1016/j.compositesa.2014.09.013
14. Schmücker M, Flucht F, Schneider H. Temperature stability of 3 M Nextel™ 610, 650, and 720 fibers – a microstructural study. In: Krenkel W, Naslain R, Schneider H, editors. High temperature ceramic matrix composites. Weinheim, FRG: Wiley-VCH; 2001. p. 73–8.
15. Parthasarathy TA, Zawada LP, John R, Cinibulk MK, Kerans RJ, Zelina J. Evaluation of oxide-oxide composites in a novel combustor wall application. Int J Appl Ceram Technol. 2005;2:122–32. https://doi.org/10.1111/j.1744-7402.2005.02014.x
16. Mattoni MA, Yang JY, Levi CG, Zok FW, Zawada LP. Effects of combustor rig exposure on a porous-matrix oxide composite. Int J Appl Ceram Technol. 2005;2:133–40. https://doi.org/10.1111/j.1744-7402.2005.02015.x
17. Cantonwine PE. Strength of thermally exposed alumina fibers Part I Single filament behavior. J Mater Sci. 2003;38:461–70, https://doi.org/10.1023/A:1021867530979
18. EN 1389. Advanced technical ceramics – ceramic composites - Physical properties - Determination of density and apparent porosity. Beuth Verlag, 2003.
19. EN 658-3. Hochleistungskeramik – Mechanische Eigenschaften von keramischen Verbundwerkstoffen bei Raumtemperatur – Teil 3: Bestimmung der Biegefestigkeit. Beuth Verlag, 2002.
20. Middendorf P, Arendts FJ, Sorour M. Leichtbau. Universitätsbibliothek Stuttgart; 2017.
21. Singh AK, Mall S. Damage effects on strength and life of oxide/oxide CMC in combustion environment. In: 21st international conference on composite materials. 2017.
22. Zhang B-G, Li Y, Zhou W, Xiao P. Residual strength evolution of 2D C/C-SiC composites subjected to tensile fatigue stresses. J Ceram Sci Technol. 2017;8(1):53–8.
23. Presby MJ, Mansour R, Manigandan K, Morscher GN, Abdi F, Godines C, et al. Characterization and simulation of foreign object damage in curved and flat SiC/SiC ceramic matrix composites. Ceram Int. 2019;45:2635–43. https://doi.org/10.1016/j.ceramint.2018.10.207
24. Sørensen BF, Holmes JW, Vanswijgenhoven EL. Rate of strength decrease of fiber-reinforced ceramic-matrix composites during fatigue. J Am Ceram Soc. 2000;83:1469–75. https://doi.org/10.1111/j.1151-2916.2000.tb01412.x
25. Ramachandran K, Leelavinodhan S, Antao C, Copti A, Mauricio C, Jyothi YL, et al. Analysis of failure mechanisms of oxide – oxide ceramic matrix composites. J Eur Ceram Soc. 2022;42:1626–34. https://doi.org/10.1016/j.jeurceramsoc.2021.11.020
26. Dassios KG, Aggelis DG, Kordatos EZ, Matikas TE. Cyclic loading of a SiC-fiber reinforced ceramic matrix composite reveals damage mechanisms and thermal residual stress state. Composites, A Appl Sci Manuf. 2013;44:105–13. https://doi.org/10.1016/j.compositesa.2012.06.011
27. Bansal NP, Lamon J, editors. Ceramic matrix composites. Hoboken, NJ, USA: John Wiley & Sons, Inc.; 2014.
28. Sørensen BF, Holmes JW, Vanswijgenhoven EL. Does a true fatigue limit exist for continuous fiber-reinforced ceramic matrix composites? J Am Ceram Soc. 2002;85:359–65. https://doi.org/10.1111/j.1151-2916.2002.tb00097.x

How to cite this article: Lehnert T, Shi Y, Cepli D, Jemmali R, Wamser T, Lauer A, et al. Effect of coupon geometry and preload on flexural properties of oxide ceramic matrix composites. Int J Appl Ceram Technol. 2023;1–14. https://doi.org/10.1111/ijac.14307